IEEE Access
Multidisciplinary ⋮ Rapid Review ⋮ Open Access Journal

Received 24 May 2024, accepted 5 August 2024, date of publication 7 August 2024, date of current version 16 August 2024.

Digital Object Identifier 10.1109/ACCESS.2024.3440015

RESEARCH ARTICLE

Active Short-Circuit Strategy for PMSMs Enabling Bounded Transient Torque and Demagnetization Current

GUSTAF FALK OLSON[1], (Graduate Student Member, IEEE), ANDREI BOJOI[2], (Graduate Student Member, IEEE), PAOLO PESCETTO[2], (Member, IEEE), SIMONE FERRARI[2], (Member, IEEE), LUCA PERETTI[1], (Senior Member, IEEE), AND GIANMARIO PELLEGRINO[2], (Fellow, IEEE)

[1]Division of Electric Power and Energy Systems, KTH Royal Institute of Technology, 114 28 Stockholm, Sweden
[2]Department of Energy "G. Ferraris," Politecnico di Torino, 10129 Turin, Italy

Corresponding author: Gustaf Falk Olson (gufo@kth.se)

ABSTRACT The active short-circuit is a standard safety measure for permanent-magnet synchronous machine drives in electric vehicles, but it can lead to harmful torque and current transients. This paper introduces a mathematical and graphical method to determine the safe operating area of pre-fault current conditions, complying with user-defined torque bounds and preventing magnet demagnetization during short-circuit transients. The method incorporates an inductance-based motor model considering magnetic saturation, which is used to outline a strategy for transitioning to safe initial conditions in the minimum time for the available voltage. Experiments on a 35-kW permanent-magnet synchronous machine support the efficacy of the proposed strategy, offering promise for its use in automotive propulsion where compliance to safety standards such as the ISO 26262 is paramount.

INDEX TERMS Active short-circuit, cross saturation, demagnetization, direct flux-vector control, PMSM.

I. INTRODUCTION

Ensuring fail-safe operation of electric vehicles (EVs) is imperative for compliance with functional safety standards such as ISO26262 [1]. An active short-circuit (ASC) is a protective measure in permanent-magnet synchronous machine (PMSM) inverters, triggered to prevent catastrophic failure [2], [3], [4], [5]. E.g. in EVs, a high-level control unit may activate the ASC due to battery overheating or brake failure. Although an inverter shutdown is preferred to an ASC, it is not applicable across all speeds due to the risk of harmful uncontrolled generation (UCG) [6].

The transition from regular operation to ASC is crucial, as the transient currents can lead to irreversible permanent magnet (PM) demagnetization and damage the inverter. Additionally, the concurrent torque pulsations may endanger the driver or stress mechanical structures [4]. Given the economic and safety risks associated with an ASC, it necessitates meticulous testing and may impose undesirable design-space constraints to mitigate potential damages [4], [7].

Several methods have been developed to evaluate transient short-circuit currents [3], [4]. These methods provide insights into demagnetization risk, torque pulsation estimation, and their dependency on electrical parameters, initial conditions, and saturation. A general conclusion is that the peak transient current increases with the loading, as a result of the increased flux linkage magnitude along the maximum-torque-per-ampere (MTPA) trajectory [5]. Ref. [3] further demonstrates that magnetic saturation greatly impacts the transient, emphasizing the importance of modeling the machine's (cross-) saturation. To this end, a flux-map-based evaluation is carried out in [5]. Contrary to [3], it introduces a general method to compute state-variable and output trajectories at non-linear magnetic conditions during the ASC transient. The results evidence how the saliency, PM magnetization, and initial loading affect the peak transient current. A method to find the hyper worst-case short-circuit current is proposed. However, this value is

The associate editor coordinating the review of this manuscript and approving it for publication was Suman Maiti.

overly conservative, assuming a lossless, undamped decay of the flux linkages at constant speed.

To suppress peak currents during ASC, [2] proposes an active method to lower the peak transient demagnetization current without using a machine model. Still, it assumes that the process is initiated at no-load, which is an optimistic scenario. Ref. [8] reduces peak current and torque without requiring feedback signals, although effectiveness decreases at lower speeds. It enters and exits ASC and open-switch conditions until the d-current reaches the characteristic current, where the ASC is clamped. Unfortunately, no method for assessing the strategy's transient torque and current from an arbitrary initial condition is proposed.

In [9], we presented a graphical/mathematical method to determine a set of initial current vectors, ensuring that the ASC trajectory obeys demagnetization and torque bounds until reaching a steady state. Knowing this safe operating area (SOA) is vital for devising effective strategies to mitigate the detrimental ASC effects because once initiated, state trajectory control becomes impossible. The model's ability to replicate the current and torque trajectories is crucial for such a strategy's effectiveness.

This paper elaborates on the method in [9] relying on offline calculations using flux maps to account for magnetic saturation. The main supplement is a strategy to transition into the SOA from any initial condition. It profits from direct flux-vector control (DFVC) and can be tuned accurately to accomplish the transition within a fixed time; the shortest achievable using the assigned voltage resources. Experiments verify the strategy's effectiveness and corroborate the accuracy of the calculated SOA.

The paper's structure is as follows: Section II details the flux-map-based short-circuit model. Section III introduces the proposed method for computing feasible initial conditions of the ASC. Section IV describes the pre-ASC control strategy, and Section V verifies it experimentally for an automotive PMSM. Finally, conclusions are drawn in Section VI.

II. SHORT-CIRCUIT MODEL BASED ON FLUX MAPS

First, the flux-map-based non-linear model of a PMSM is introduced. By selecting the dq-currents as state variables, their dynamics are obtained without inverse flux maps and the electromechanical torque equation is easily applied. These virtues facilitate developing and implementing the ASC strategy presented later. The section ends by explaining the calculations of steady-state short-circuit current (SSC) and torque.

A. STATE-SPACE MODEL

The stator voltage equation in (1) and flux linkage equation in (2) dictate the electrical dynamics of a PMSM.

$$\bar{u}_{dq} = \boldsymbol{R}_s \bar{i}_{dq} + \frac{d\bar{\psi}_{s,dq}}{dt} + \omega_r \boldsymbol{J} \bar{\psi}_{s,dq} \tag{1}$$

$$\bar{\psi}_{s,dq} = \boldsymbol{L}_s \bar{i}_{dq} + \bar{\psi}_{r,dq} \tag{2}$$

Here, $\bar{u}_{dq}$, $\bar{i}_{dq}$ and $\bar{\psi}_{s,dq}$ are the real-valued stator voltage, current, and flux linkage space-vectors. ω_r is the rotor electrical speed, which relates to the mechanical speed, ω_m, and pole-pair number, p, as $\omega_r = p\omega_m$. The bold font letters denote matrices. Specifically, $\boldsymbol{R}_s = \mathrm{diag}\left([R_s, R_s]\right)$ is the stator resistance matrix, $\boldsymbol{L}_s = \mathrm{diag}\left([L_d, L_q]\right)$ is the inductance matrix, and $\boldsymbol{J}$ is a $\pi/2$ rad rotation matrix. Unless the rotor is isotropic, as in a surface PM machine, $L_d \neq L_q$. Adopting the PM-convention as the definition of the dq-axes orientation, the rotor flux linkage is $\bar{\psi}^T_{r,dq} = [\psi_{PM},\ 0]$, where ψ_{PM} denotes the PM flux linkage. Hence, $\bar{e}^T_{dq} = [0,\ \omega_r \psi_{PM}]$ becomes the back-electro-motive force (emf).

To model the non-linearities of the d- and q-axes flux linkages, ψ_d and ψ_q, invoked by the magnetic steel saturation, flux maps can be identified as functions of $\bar{i}_{dq}$ [10], [11]. They constitute lookup tables, generally defined as in (3), where the boldface symbols represent lookup tables with the inputs within parentheses.

$$\begin{cases} \psi_d = \boldsymbol{\Psi_d}(i_d, i_q) \\ \psi_q = \boldsymbol{\Psi_q}(i_d, i_q) \end{cases} \tag{3}$$

When the machine experiences saturation, the voltage equations, (1), must account for the time derivatives of the current-inductance products and PM flux. The governing state-space equation, (4), results from the product rule for derivatives.

$$\frac{d\bar{i}_{dq}}{dt} = \boldsymbol{L}_{nl}^{-1}\left(\underbrace{\begin{bmatrix} -R_s & \omega_r L_q \\ -\omega_r L_d & -R_s \end{bmatrix}}_{\boldsymbol{A}} \bar{i}_{dq} + \bar{u}_{dq} - \bar{e}_{dq} \right), \tag{4}$$

$$\boldsymbol{L}_{nl}(i_d, i_q) = \begin{bmatrix} L_{nl,11}(i_d, i_q) & L_{nl,12}(i_d, i_q) \\ L_{nl,21}(i_d, i_q) & L_{nl,22}(i_d, i_q) \end{bmatrix},$$

$$L_{nl,11} = \frac{\partial L_d}{\partial i_d} i_d + L_d + \frac{\partial \psi_{PM}}{\partial i_d}, \quad L_{nl,21} = \frac{\partial L_q}{\partial i_d} i_q,$$

$$L_{nl,12} = \frac{\partial L_d}{\partial i_q} i_d + \frac{\partial \psi_{PM}}{\partial i_q}, \quad L_{nl,22} = \frac{\partial L_q}{\partial i_q} i_q + L_q$$

The chord-slope inductances $L_x(i_d, i_q) \triangleq \boldsymbol{\Psi}_x(i_d, i_q)/\boldsymbol{I}_x$, are functions of $\bar{i}_{dq}$ with domains defined by the current grids $\boldsymbol{I}_d$ and $\boldsymbol{I}_q$. Consequently, they also establish the domains of the identified flux maps. Henceforth, the arguments of the parameter maps are omitted to improve readability. The required partial derivatives of the chord-slope inductances and PM flux linkages can readily be found using finite differences on the manipulated flux maps.

Finally, an average torque map is calculated from element-wise multiplication of the flux maps and current grids:

$$\boldsymbol{\tau}_e = 1.5p\left(\boldsymbol{\Psi}_d \odot \boldsymbol{I}_q - \boldsymbol{\Psi}_q \odot \boldsymbol{I}_d\right). \tag{5}$$

B. STEADY-STATE SHORT-CIRCUIT CURRENT

The SSC at a fixed speed is obtained by setting $d\bar{i}_{dq}/dt = \bar{u}_{dq} = 0$ in (4). Since the flux-map-based model lacks an analytical solution, the Gauss-Newton method, (6), is applied to solve for the SSC. It updates the initial guess, $\bar{i}^{(0)}_{dq}$, of the SSC until some condition is met at iteration k. E.g. the

criterion $\|\Delta\bar{i}_{dq}^{(k)}\|_2 < \epsilon$ can be used for some scalar $\epsilon > 0$.

$$\bar{i}_{dq}^{(k+1)} = \bar{i}_{dq}^{(k)} - \underbrace{\mathbf{J}^{-1}\left(\bar{i}_{dq}^{(k)}\right)\bar{f}\left(\bar{i}_{dq}^{(k)}\right)}_{\Delta\bar{i}_{dq}^{(k)}}, \tag{6}$$

$$\bar{f}\left(\bar{i}_{dq}^{(k)}\right) = \boldsymbol{A}\bar{i}_{dq} - \bar{e}_{dq}, \quad \mathbf{J}\left(\bar{i}_{dq}^{(k)}\right) = \begin{bmatrix} \frac{\partial f_1}{\partial i_d} & \frac{\partial f_1}{\partial i_q} \\ \frac{\partial f_2}{\partial i_d} & \frac{\partial f_2}{\partial i_q} \end{bmatrix},$$

$$\begin{aligned} \frac{\partial f_1}{\partial i_d} &= -R_s + \omega_r i_q \frac{\partial L_q}{\partial i_d}, \quad \frac{\partial f_2}{\partial i_d} \\ &= -\omega_r \left(L_d + \frac{\partial L_d}{\partial i_d} i_d + \frac{\partial \psi_{PM}}{\partial i_d} \right) \\ \frac{\partial f_1}{\partial i_q} &= \omega_r \left(L_q + \frac{\partial L_q}{\partial i_q} i_q \right), \quad \frac{\partial f_2}{\partial i_q} \\ &= -R_s - \omega_r \left(i_d \frac{\partial L_d}{\partial i_q} + \frac{\partial \psi_{PM}}{\partial i_q} \right) \end{aligned}$$

TABLE 1. Parameters of the BRUSA HSM1-6.17.12 with series-connected three-phase sets.

Phases	m_s	3	[-]
Pole pairs	p	3	[-]
Nominal power	P_N	35	[kW]
Nominal/Peak speed	$\omega_{m,N}$ / $\omega_{m,\mathrm{pk}}$	1′800 / 6′000	[rpm]
Nominal/Peak torque	τ_N / τ_pk	130 / 320	[Nm]
Nominal current	I_N	250	[A_{pk}]
DC-link voltage	V_{dc}	400	[V]
Stator resistance	$R_s(25\,^\circ\mathrm{C})$	55	[mΩ]
Critical UCG speed	$\omega_{m,\mathrm{UCG}}(\alpha = 1)$	5′300	[rpm]
PM flux linkage	ψ_{PM}	148.6	[mVs]

The Jacobian, $\mathbf{J}\left(\bar{i}_{dq}\right)$, of the function $\bar{f}\left(\bar{i}_{dq}\right)$ in (6) is obtained from the flux-maps and the current state and can be supplied directly to the Gauss-Newton algorithm. The SSC is obtained as $\bar{i}_{dq}^{(K+1)}$ when the stopping condition is fulfilled after iteration $k = K$ and the torque results from (5).

III. ACTIVE SHORT-CIRCUIT: SAFE INITIAL STATES

To comply with safety demands and protect the PMs from demagnetization, two constraints on the ASC transient are acknowledged, namely not to exceed: (1) the demagnetization current, $|i_{d,\mathrm{demag}}|$, and (2) a user-defined maximum torque $|\tau_{e,\max}|$ during the transient. Hence, we first describe the machine under test (MUT) in Section III-A. Section III-B declares the speed criterion that warrants an ASC in place of an inverter shutdown and reviews the MUT's demagnetization limit. Section III-C reviews the MUT's dynamics during an ASC. Section III-D treats the demagnetization objective and Section III-E the torque objective. Lastly, Section III-F considers the impacts of speed variations.

A. MACHINE UNDER TEST

The MUT in this study is the 70 kW commercial three-phase interior PMSM BRUSA HSM1-6.17.12 [12], henceforth used as a working example. Its nameplate parameters are declared in Table 1. The flux maps of the MUT were identified experimentally using the method in [13] for the current ranges $i_d \in [-230,\ 40]$ A and $i_q \in [0,\ 40]$ A. The inverter's continuous current limit of $I_N = 250$ A, which is lower than the rated current of the MUT, limited the current domain. Subsequently, the maps were extended into the negative i_q-domain, assuming symmetry about the q-axis. Apparent inductances are derived from the obtained flux maps, whereas ψ_{PM} is found from an open-circuit test. The incremental inductances, l_{xy} in (4), are computed from finite differences of the apparent inductance maps.

B. UNCONTROLLED GENERATION AND DEMAGNETIZATION LIMITS

Inverter shutdown occurs when all inverter switches are off, and is preferable to an ASC if the induced back-emf is below the reflected DC-link voltage. Exceeding this voltage turns on anti-parallel diodes, leading to UCG [6]. The critical speed for this condition, listed in Table 1, is given by:

$$\omega_{m,\mathrm{UCG}} = \alpha \frac{2}{\pi} \frac{V_{dc}}{p\psi_{PM}}, \quad \alpha = \begin{cases} (2\sqrt{\xi - 1})/\xi, & \xi > 2 \\ 1, & \xi \leq 2. \end{cases} \tag{7}$$

Here, α represents a speed derating factor set to unity in the table due to saliency variability. It accounts for the bistable UCG operation mode reported in [6], where the diodes remain forward biased until the speed drops by $(1 - \alpha)$. Notably, $\omega_{m,\mathrm{UCG}}(\alpha = 1)$ exceeds the nominal speed of the MUT. Setting $\xi = 4$ reduces it by 15 %. In practice, inverter shutdown is thus preferred over an ASC unless operating in deep field weakening.

During an ASC, the machine's PMs may partially demagnetize if the current trajectory crosses the demagnetization limit (negative d-current). This limit depends on PM type, mounting, and temperature [14, Ch. 3.7.4]. The MUT's datasheet does not declare a demagnetization limit. With a heuristic approach, we can, however, crudely estimate it from simulations using (4) for which linear extrapolation is applied to expand the domain of the experimental flux maps. Assuming the PMs withstand an ASC at nominal speed and maximum torque when operated at the MTPA, the minimum d-current during such a transient is $|i_{d,\mathrm{demag}}|$ =650 A.

Thus, the machine seems designed to endure higher demagnetization currents than the installed inverter limits (Table 1). For illustration, we, therefore, set a fictive demagnetization limit of $i_{d,\mathrm{demag}} = -200$ A, providing a 20-% margin to I_N. This methodology serves as a proof-of-concept; the actual demagnetization limit likely exceeds the adopted one.

C. PHASE PORTRAIT OF THE ASC TRANSIENT

Once the ASC begins, $\bar{u}_{dq} = 0$ and the drive loses control over the system dynamics, (4) and $\bar{e}_{dq}$ becomes the sole driving force. Consequently, only the initial value, $\bar{i}_{dq}(0)$, influences the current vector's trajectory at constant speed. We now define an acceptable ASC transient and explore how to determine initial values for such transients.

The flux maps and R_s fully characterize the state dynamics and electromechanical output of the PMSM. Thus, the ASC phase portrait in Fig. 1 is generated by applying (4) at $\bar{u}_{dq} = 0$. It depicts the time-derivative vector field of $\bar{i}_{dq}$ at a fixed speed, 1500 rpm, and winding temperature, 25 °C. For illustrative purposes, the field is color-coded:

- Yellow: $di_d/dt \geq 0$ and $di_q/dt \geq 0$.
- Orange: $di_d/dt \geq 0$ and $di_q/dt < 0$.
- Violet: $di_d/dt < 0$ and $di_q/dt \geq 0$.
- Blue: $di_d/dt < 0$ and $di_q/dt < 0$.

The phase-portrait includes the demagnetization limit, $i_{d,\text{demag}} < 0$, the inverter current limit, $I_{\max}$ (de-rated to coincide with $i_{d,\text{demag}}$), and the SSC at the evaluated speed to depict operational boundaries. An MTPA trajectory illustrates typical operating points under field-oriented control (FOC). Evidently, the current derivatives increase with loading, leading to wider spiraling trajectories towards the SSC, as indicated by the dotted brick-colored infeasible trajectory. Thus, transient demagnetization current increases with loading, consistent with the Monte Carlo simulation in [3] and analytically confirmed in [5].

D. DEMAGNETIZATION LIMIT SOA

The demagnetization boundary is not exceeded if $di_d/dt\,(i_{d,\text{demag}}, i_q) \geq 0$ whenever the ASC trajectory touches the demagnetization boundary. Hence, we locate $di_d/dt\,(i_{d,\text{demag}}, i_q) = 0$ along the line $i_d = i_{d,\text{demag}}$ in the phase portrait to delineate the safe state-space regions.

For constant $i_d = I_d$, $\text{sgn}\,(di_d(I_d, i_q)/dt)$ changes once along the lines (I_d, i_q). This is an effect of the stable lossy dynamics of (4), where currents spiral monotonically to the SSC [5]. $\mathbf{L}_{nl}^{-1}$ in (4) prohibits an analytical solution, $(i_{d,\text{demag}}, i_{q,\text{demag}})$, fulfilling $di_d/dt > 0$ for $i_d = i_{d,demag}$ so the solution is found numerically.

It serves as initial values for an ordinary differential equation (ODE) solver employing interpolated inductance maps for accurate derivatives. The trajectory when stepping backward in time defines a new boundary. With the demagnetization and inverter current limits, it demarcates a SOA marked in green in Fig. 1, whose interior ensures $i_d(t) > i_{d,\text{demag}}\ \forall t > 0$ once the ASC is initiated.

Interestingly, the demagnetization SOA-boundary stays close to the iso-flux line $|\bar{\psi}_s| = 50$ mVs, coherent with findings in [5]. Thus, the SOA boundary closely tracks an iso-flux line for short durations, especially when resistive and magnetic losses are small. Approximating the SOA boundary as the smallest flux-linkage amplitude enclosed by the computed boundary (∼40 mVs) proves practically fruitful when adopting DFVC in Section IV-A for the proposed ASC strategy.

E. TORQUE LIMIT SOA

The procedure to delimit the SOA for the torque follows the same line of thought as delimiting the SOA for the demagnetization current but involves more calculations. We recall that the SOA is the set of initial conditions $\bar{i}_{dq}(0)$ that results in a current trajectory obeying $|\tau_e(t)| \leq \tau_{e,\max}\ \forall t > 0$ at a fixed speed and temperature.

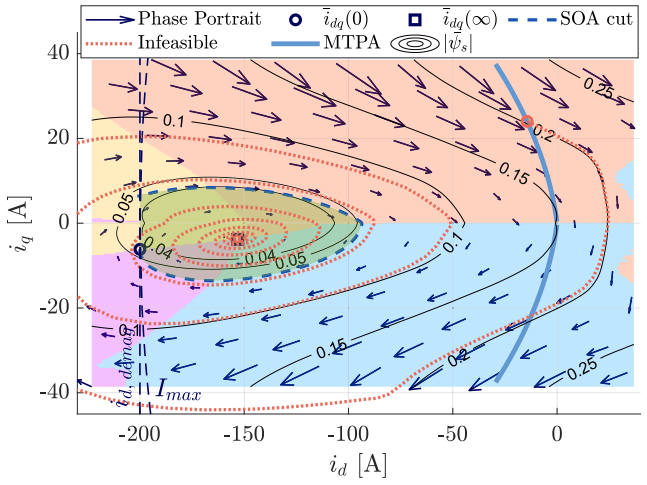

FIGURE 1. Phase-portrait at $\omega_m = 1500$ rpm with the SOA (green) honoring the demagnetization and inverter current limit. Iso-flux lines are shown in Vs and the maximum iso-flux line that fits within the SOA, $|\bar{\psi}_s| = 40$ mVs, is included.

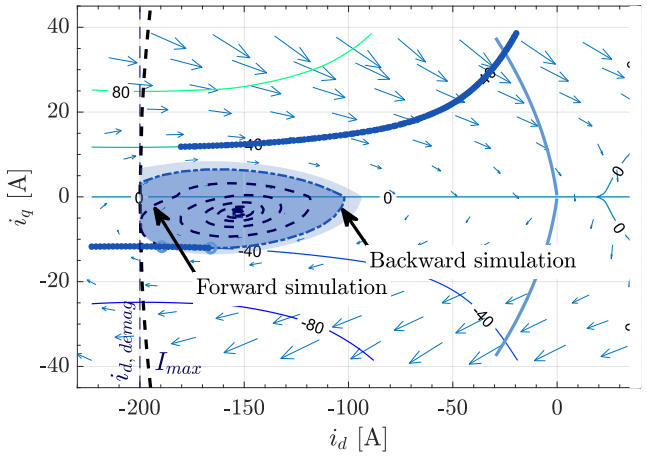

FIGURE 2. Phase portrait at $\omega_m = 1500$ rpm with the SOA of the demagnetization limits (light shade) and the torque (dark shade). The SSC is marked with a square, and the MTPA-trajectory is solid in sky blue. The iso-torque lines are labeled with τ_e in Nm.

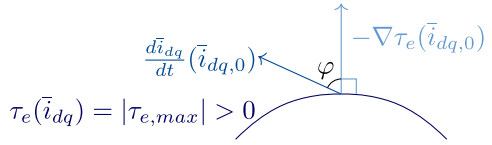

FIGURE 3. Illustration of the gradient condition, (8), for the torque constraint.

Fig. 2 plots the iso-torque lines of the MUT. The requirement for all $\bar{i}_{dq}$ resulting in $|\tau_e(\bar{i}_{dq})| = \tau_{\max}$ is formally equivalent to:

$$\begin{cases} \nabla\tau_e(\bar{i}_{dq}) \cdot \dfrac{d\bar{i}_{dq}}{dt} \geq 0, & \text{if } \tau_e < 0 \\ -\nabla\tau_e(\bar{i}_{dq}) \cdot \dfrac{d\bar{i}_{dq}}{dt} \geq 0, & \text{if } \tau_e > 0. \end{cases} \tag{8}$$

Eq. (8) is a gradient condition illustrated in Fig. 3. Since $\nabla\tau_e$ is perpendicular to the iso-torque line, the torque does not increase at the next time-step if the current-derivative vector points inwards from the $\tau_{\max}$-curve. This constraint is expressed in (8), where the angle φ between $\pm\nabla\tau_e(\bar{i}_{dq})$ and $d\bar{i}_{dq}/dt$ must obey $\varphi \in [-\pi/2,\ \pi/2]$. A procedure to find the torque SOA is now formulated. Fig. 2 is provided as a reference with $\tau_{e,\max} = 40\,\text{Nm}$, corresponding to 13 % of the MUT's peak torque.

1) Find the set of $\bar{i}_{dq}$ along one of the iso-torque curves $\pm\tau_{e,\max}$ that obeys (8), corresponding to the blue solid markers in Fig. 2.
2) Step forward and backward from the first and last point obeying (8) (both circled in sky blue) until a torque or demagnetization limit is intersected.
3) The generated trajectories, the current-limit circle, and demagnetization limits constitute new boundaries.
4) Repeat 1-3 for all four iso-torque lines. The innermost, most restrictive, among all boundaries is retained and updated between the simulations so that an enclosing boundary always exists.

The intersection of the calculated torque and demagnetization limits constitutes the ultimate SOA shaded in dark blue.

It is seen that the demagnetization limit entirely encloses the safe torque region. Consequently, the torque constraint is the limiting factor for the SOA in this example. In this example, the worst-case torque starting at the demagnetization boundary is only 5.7 Nm (1.8 % of the peak torque) higher than the imposed boundary, which is found acceptable. Therefore, we relax the torque constraint and impose the demagnetization limit, shaded in light blue in Fig. 2, as the ultimate SOA at 1500 rpm.

The ASC transient typically settles to the SSC within hundreds of milliseconds, with a temporary overcurrent only lasting a fraction of that time [3]. This temporary overcurrent may be acceptable. If necessary, de-rating the demagnetization boundary acts to limit the current.

F. EFFECTS OF SPEED VARIATIONS

Higher speeds cause the SOA to contract due to an increased driving force (back-emf). This is demonstrated in Fig. 4 for (a) demagnetization and (b) torque boundaries (−200 A and 70 Nm, respectively). The SOA in the demagnetization plot reduces significantly from $\omega_m = 500\,\text{rpm}$ to $\omega_m = 1000\,\text{rpm}$, with a smaller decline from $\omega_m = 1000\,\text{rpm}$ to $\omega_m = 3000\,\text{rpm}$, attributed to the greater impact of the resistive voltage drop at low speeds. In contrast, Fig. 4b exhibits an opposite effect on the torque SOA, with higher speeds resulting in a larger SOA. However, this expansion diminishes as speed increases, akin to the demagnetization SOA. As ASCs are mainly applied at high speeds, the combined SOA remains relatively fixed for applicable speeds.

During ASC transients, speed variations are anticipated. They are particularly influenced by the vehicle's inertia, implying they are likely to be small in heavy vehicles. When the vehicle decelerates, SOA boundaries remain conservative estimates. Fig. 5 depicts the torque's time-derivative in state space during an ASC. Orange areas indicate a torque decrease, whereas blue indicates an increase. For most initial operating points within the SOA and all points on the MTPA trajectory, torque initially declines. Consequently, a forward-moving vehicle loses thrust, enters braking, or applies more braking torque at the start of the ASC, leading to a likely speed drop unless on a sufficiently steep downhill. Conversely, the torque rises if the ASC starts in blue areas. To avoid such situations, areas where $d\tau_e/dt > 0$ could possibly be excluded from the SOA.

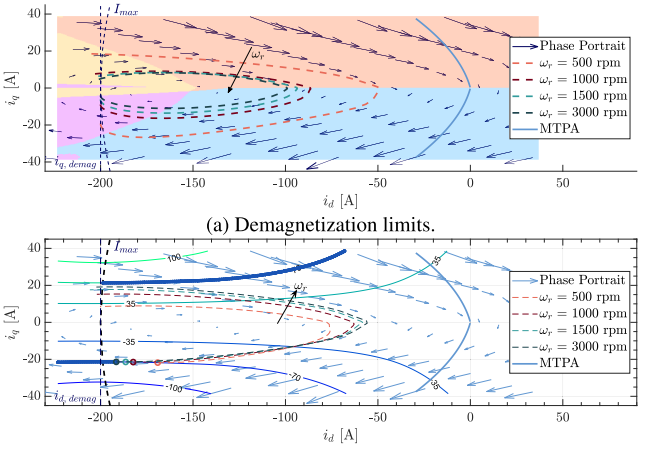

(a) Demagnetization limits.

(b) Torque limits. Circles indicate the largest i_d for which (8) holds at each considered speed.

FIGURE 4. SOA boundaries for different speeds. The phase portraits are drawn for $\omega_m = 3000\,\text{rpm}$.

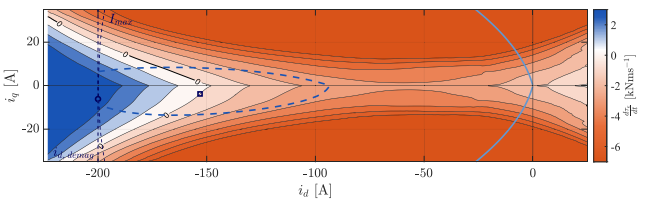

FIGURE 5. Time derivative of the torque in state-space with demagnetization SOA (blue dashed), MTPA trajectory (sky solid), and SSC (navy square) at $\omega_m = 1500\,\text{rpm}$.

IV. PRE-ASC CONTROL STRATEGY

The ISO26262 standard defines the fault tolerant time interval (FTTI) as the total elapsed time between a fault's occurrence and the initiation of a hazardous event [1]. Consequently, the system must detect it and enter a fail-safe state within the FTTI. Considering that all states within the SOA are feasible initial conditions for an ASC, $\bar{i}_{dq}(0)$, the regulator can be used to transition the state vector into the SOA before applying the ASC.

In the coming section, the DFVC is introduced. With minimal intervention to the controller's interrupt service routine, an algorithm consisting of a few lines of code is proposed that can be inserted into the existing control code. The selection of user-defined variables and their effect on the speed and robustness of the transient into the SOA is discussed.

A. DIRECT FLUX-VECTOR CONTROL

DFVC is a type of stator-field oriented control strategy where the rotating orthogonal $d_s q_s$-frame aligns its d_s-axis with the stator flux-linkage space vector, as illustrated in Fig. 6. The flux-linkage magnitude, ψ_s^{sf}, and the q_s current, i_q^{sf}, are the controlled states governed by (9), where the parameters k and b depend on the instantaneous load angle, $\delta_{sr} = \tan^{-1}(\psi_q/\psi_d)$, and stator flux-linkage [15].

$$\frac{d\psi_s^{\mathrm{sf}}}{dt} = v_d^{\mathrm{sf}} - R_s i_d^{\mathrm{sf}} \tag{9a}$$

$$\frac{di_q^{\mathrm{sf}}}{dt} = \frac{-R_s i_q^{\mathrm{sf}} + k\left(v_d^{\mathrm{sf}} - R_s i_d^{\mathrm{sf}}\right) + b\left(v_q^{\mathrm{sf}} - \omega_{re}\psi_s^{\mathrm{sf}}\right)}{L_d} \tag{9b}$$

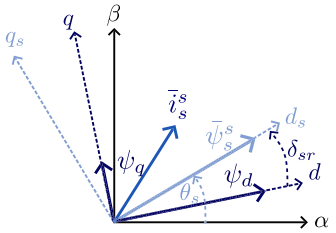

FIGURE 6. Reference-frame relations. Stator-flux oriented: $d_s q_s$. Rotor-flux oriented: dq.

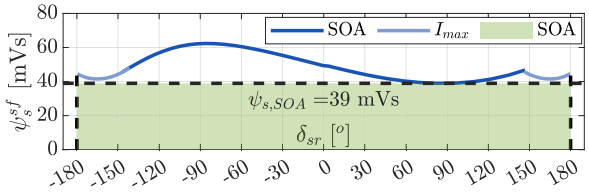

FIGURE 7. Conservative demagnetization SOA in $[\psi_s^{\mathrm{sf}}, \delta_{sr}]$ state-space for $i_{d,\mathrm{demag}} = -200$ A.

Importantly, the flux-amplitude dynamics, (9a), are decoupled. Therefore, P-control is sufficient to obtain first-order closed-loop dynamics with the proportional gain setting the closed-loop bandwidth, $\alpha_{\psi,BW}$, [15]. An integral term can be introduced to improve the steady-state disturbance rejection with retained closed-loop dynamics.

The image of the $\bar{i}_{dq}$ SOA boundary in the $[\psi_s^{\mathrm{sf}},\ i_q^{\mathrm{sf}}]^T$ state space is obtained from the transformations in (10) and plotted in Fig. 7. Eq. (3) maps the rotor-field oriented currents to the flux linkages in an intermediate step.

$$\psi_s^{\mathrm{sf}} = \|\bar{\psi}_{dq}\|_2 \tag{10a}$$

$$i_q^{\mathrm{sf}} = \cos(\delta_{sr}) i_q - \sin(\delta_{sr}) i_d \tag{10b}$$

The boundary is selected conservatively as the minimum iso-flux-linkage circle that fits within the computed SOA (Fig. 7a). In the stator-flux state-space, such a circle transforms into a constant flux-linkage level for all load angles, Fig. 7b. As a result, the SOA is independent of i_q^{sf}. and only one scalar needs to be stored in memory per considered speed, relieving memory usage as compared to implementing the strategy using conventional rotor-FOC for $\bar{i}_{dq}$.

With the preliminaries set, we propose an ASC strategy, minimizing code changes to the existing DFVC. The strategy logic in Alg. 1 precedes the stator-flux reference assignment, $\psi_s^{\mathrm{sf}*}$. A high-level block diagram of the adapted drive is drawn in Fig. 8, while the details of the hybrid flux observer are shown in Fig. 9 [16]. Circumflexes mark estimates and complex stator reference-frame vectors are denoted as $x_s^s = x_{\alpha\beta} = x_\alpha + jx_\beta$ for a generic quantity x.

Algorithm 1 Proposed ASC strategy in DFVC. A high-level control unit triggers *Fault* and $\psi_s^{\mathrm{sf}*}$ decreases. When the SOA is reached the ASC initiates by assigning *true* to ascFlag.

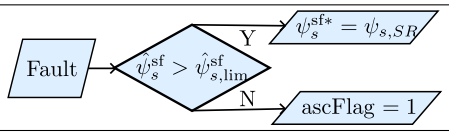

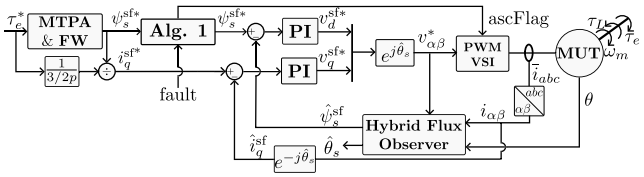

FIGURE 8. Block-diagram of the DFVC including the proposed ASC strategy in the block Alg. 1. VSI denotes the voltage source inverter and FW denotes field-weakening strategy.

The strategy works as follows: When a high-level control unit detects a fault, $\psi_s^{\mathrm{sf}*} = \psi_{s,\,\mathrm{SR}}$ sets the flux regulator reference, while $i_q^{\mathrm{sf}*}$ remains unchanged. In principle, it is advisable to limit the flux reduction-time to more than the DC-link voltage, V_{dc}, allows. Firstly, a portion of V_{dc} may be assigned to the continued regulation of i_q^{sf}. Secondly, limiting the voltage enables a deterministic reduction of the flux linkage's undershoot. Therefore, we introduce $v_{d,\mathrm{lim}}^{\mathrm{sf}}$ as the maximum applicable d-axis voltage, setting the flux-decay rate in Vs/s. If the parameter $\psi_{s,\,\mathrm{SR}}$ in Alg. 1 fulfills (11), a pure P-controller directly imposes $v_{d,\mathrm{lim}}^{\mathrm{sf}}$ and remains in this slew-rate limit until the application of the ASC.

$$\psi_{s,\,\mathrm{SR}} < \psi_{s,\mathrm{lim}}^{\mathrm{sf}} - v_{d,\,\mathrm{lim}}^{\mathrm{sf}}/\alpha_{\psi,BW} \tag{11}$$

When the current is sampled with a period of T_s in between the pulse width modulation (PWM) applications and a sample at time $t_{1,s} = t_1 - 0.5T_s$ results in a flux estimate of $\hat{\psi}_s^{\mathrm{sf}}(t_1) \gtrsim \psi_{s,\mathrm{lim}}^{\mathrm{sf}}$, the flux-linkage will continue to slew towards and below $\psi_{s,\mathrm{lim}}^{\mathrm{sf}}$ and *ascFlag* will not be issued until the next PWM period. Then, the maximum flux-linkage decrease between the sampling of the currents at $t_{1,s}$ and the application of the ASC is

$$\Delta\psi_{s,\mathrm{lim}}^s = 2.5\, v_{d,\mathrm{lim}}^{\mathrm{sf}} T_s. \tag{12}$$

Evidently, $\psi_{s,\mathrm{SOA}}^s - \Delta\psi_{s,\mathrm{lim}}^s$ should be far from the demagnetization limit. Moreover, if $\psi_{s,\mathrm{SOA}}^s - \Delta\psi_{s,\mathrm{lim}}^s$ is too close to zero, the field orientation, flux estimation, and control may suffer from deteriorated performance, which should be avoided. Particularly, a reliable flux estimation is required. The minimum flux linkage at which adequate

performance is retained should be evaluated case-by-case and used to determine an appropriate value of $v^{\mathrm{sf}}_{d,\mathrm{lim}}$.

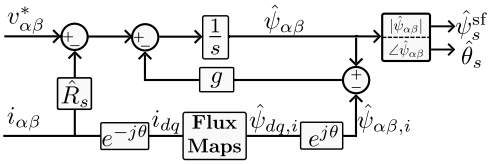

FIGURE 9. The DFVC hybrid flux observer. $1/s$ denotes integration and the scalar gain g is the cutoff rotor speed of the current model in electrical rad/s [16].

A notable aspect of the proposed DFVC pre-ASC strategy is that it renders the shortest possible duration of the transient for the available voltage, irrespective of the load angle, since all the available (assigned) voltage is used to reduce the flux-linkage in every PWM period. This may be considered an advantage also for the reference generation as compared to implementing the strategy in FOC, where an adequate $\bar{i}^*_{dq}$ needs to be generated for each pre-fault operating point for an equally effective volt-second-utilization. Unlike the uncoupled dynamics of ψ^{sf}_s in (9a), the dq-axes cross-coupling, evident from (4), also necessitates adequate cross-coupling cancellation for a well-behaved dynamic response.

V. EXPERIMENTAL VALIDATION

This section presents experimental results validating the method for determining the SOA of initial state variables before an ASC. The experiments are compared to simulations.

First, steady-state short-circuit curves of current and torque versus speed curves are shown to verify the machine model. Subsequently, transient short-circuit curves from a low speed (500 rpm) and low torque, with reduced stator flux-linkage, are demonstrated. As the initial condition is within the SOA, the ASC can be applied directly.

Next, the machine operates in DFVC along the MTPA curve at a higher speed (1500 rpm). In this scenario, ψ^{sf}_s must be reduced using the methodology outlined in Section IV-A to confine the current trajectory within the feasible state-space region before ASC application. Controller actions are simulated and contrasted to the measurements. A simulation of an ASC without preventive actions is appended.

A. TEST RIG SETUP

The test rig of the experimental validation is reported in Fig. 10. The MUT (Brusa HSM1-6.17.12 motor) is on the left, while the driving-machine (DM) is an induction machine (IM) rated 22 kW, 100 Nm (nominal). From the picture, the 600 A Ultrastab LEM current transducers, used to measure the MUT phase currents are visible on the top-right, while a 200-Nm HBM T40B torquemeter is connected between the MUT and the DM to measure the shaft torque and speed. An HBK Gen7t data recorder with direct line voltage pick-up completes the data-acquisition system (DAQ).

The MUT is an open-end-winding dual three-phase PMSM with various connection possibilities. In these tests, the windings were connected in series obtaining an equivalent 3-phase motor, whose parameters are listed in Table 1. Notably, V_{dc} stays at the nominal level of the dual three-phase machine, resulting in halved speed and power ratings.

The driveline includes an inverter generating gate signals through space-vector PWM implemented on a dSPACE 1202 MicroLabBox using DFVC with the PI-controller parameters in Table 2. An ASC is activated by setting the duty cycle of either all upper or lower insulated gate bipolar transistors (IGBTs) of the two-level inverter to 100 %.

TABLE 2. Controller parameters.

$K_{P,\psi}$ [$\frac{\mathrm{rad}}{\mathrm{s}}$]	$K_{I,\psi}$ [$\frac{\mathrm{rad}}{\mathrm{s}^2}$]	K_{P,i_q} [Ω]	K_{I,i_q} [$\frac{\Omega}{\mathrm{s}}$]	$v^{\mathrm{sf}}_{d,\mathrm{lim}}$ [V]	F_s [kHz]
300π	$K^2_{P,\psi}/10$	$K_{P,\psi}L_q$	$K_{I,\psi}L_q$	50	5

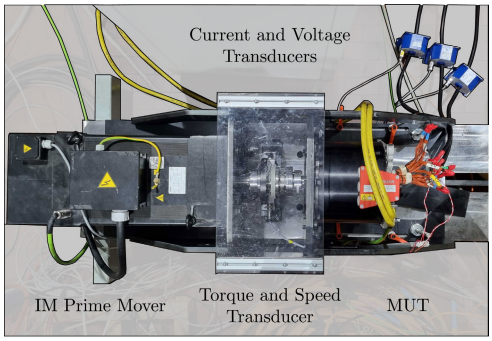

FIGURE 10. Photo of the MUT and DM on the test rig.

B. SYR-E DRIVE SIMULATIONS

The open-source platform SyR-e [17] provides a combined machine design and FEA simulation environment based on FEMM® and Matlab®. Besides these capabilities, SyR-e embeds routines for the flux maps elaboration, with possibilities to simulate dynamic drive models with the syreDrive feature [18], [19]. It seamlessly generates a Matlab®/Simulink® model of the entire drive, with deployable C control code. This feature allows for validating the control algorithm before experiments and comparing the simulated dynamic model and the actual drive, including inverter non-idealities as dead times and IGBT voltage drops, one-to-one.

The aforementioned non-idealities of the inverter IGBTs and its anti-parallel diodes result in a residual voltage on the machine terminals during the steady-state short circuit [10]. It is incorporated in the dynamic simulations by adopting the inverter parameters in Table 3. In the steady-state short-circuit condition, the resulting terminal line-to-line phase voltages simulated at 1500 rpm are compared to the experimentally obtained counterparts in Fig. 11.

C. STEADY-STATE SHORT CIRCUIT TEST

Fig. 12 compares measured SSC and torque with those computed from the identified flux maps. With speed imposed

by the DM and recorded by the DAQ at each steady-state operating point, the SSC is calculated using (6). The flux maps then determine the steady-state torque using (5). The model predicts a 2.9 Nm/3.5 % lower peak breaking (absolute) torque at speed approximately 15 rpm higher than observed. At 700 rpm, the current amplitude has almost converged to the characteristic current, measuring 148.6 A; about 2.4 % lower than model prediction. Both the current amplitude and torque align well, especially above peak torque speed.

TABLE 3. Inverter model parameters.

IGBT forward voltage	$V_{f,\mathrm{IGBT}}$	0.80	[V]
IGBT on-resistance	$R_{\mathrm{on,IGBT}}$	6	[mΩ]
Diode forward voltage	V_d	0.72	[V]
Diode on-resistance	R_d	7.5	[mΩ]

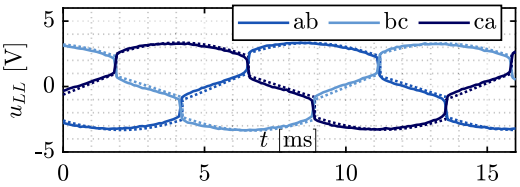

FIGURE 11. Terminal line-to-line voltages during a steady-state short circuit simulated in syreDrive with the parameters in Table 3 (dotted) and measured on the test-rig (solid).

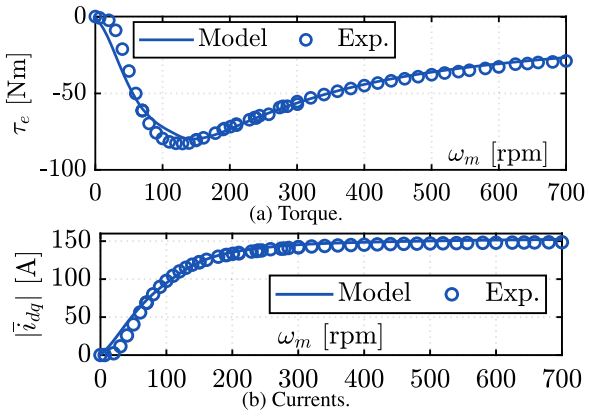

FIGURE 12. Comparing the SSC currents and torque of the experiment to the flux-map-based model.

D. TRANSIENT SHORT-CIRCUIT: STARTING IN THE SOA

At 500 rpm, $\bar{i}_{dq}^{T} = [-120, -4]$ A is a low-torque generating operation point in deep field weakening ($\psi_s^{sf} = 40$ mVs), constituting a safe initial condition for the ASC transient. It was selected to validate the model during a short-circuit transient. The ASC is applied directly at this operating condition without flux reduction and the resulting torque, speed, and $\bar{i}_{dq}$ currents are shown in Fig. 13 together with

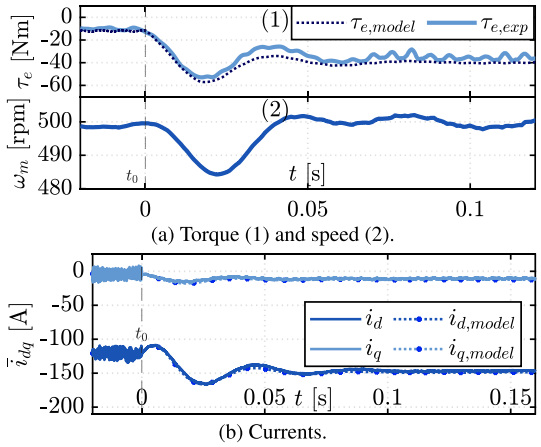

FIGURE 13. Comparing the transient currents and torque of the experiment to the flux-map-based model. The MUT was operated in DFVC with zero initial torque and reduced field using the references $\psi_s^{*sf} = 40$ mVs.

the simulated trajectories. The speed profile in Fig. 13a is imposed in the SyR-e Drive simulation to account for the post-ASC speed disturbances. Overall, the simulated current and torque correspond closely to the measurements. The minimum torque is approximately 9.4 % smaller in the simulation as is the steady state short-circuit torque. The maximum errors of the currents are 5.1 A (3.8 %) and 2.9 A (19.5 %) for the d- and q-current, respectively, confirming the model's accuracy during transient short-circuits.

E. ASC STRATEGY IMPLEMENTATION FROM MTPA

In the previous section, the ASC was initiated from a safe initial state. In contrast, the fault flag is now issued when the machine runs at an operating point of [$\omega_m = 1500$ rpm, $\tau_e = 21$ Nm] on the MTPA curve. The controller references at this operating point are [$\psi_s^{\mathrm{sf}*} = 0.2$ Vs, $i_q^{\mathrm{sf}*} = 26$ A]. Directly applying the ASC at this operating point is expected to yield the brick-colored current trajectory in Fig. 14a, which was simulated using a numerical ODE solver on (4) at a constant speed (i.e. not accounting for inverter non-idealities or speed variations). The inductances were assumed to be fully saturated in the region outside the identified flux maps. It is seen that the trajectory violates the imposed maximum current limit of 200 A by 44 %. Furthermore, it gives a torque reversal of 140 Nm, corresponding to more than the MUT's nominal torque, in 6 ms.

To constrain the current within the prescribed boundary of 200 A, Fig. 7 indicates that the SOA is reached for a flux-linkage of $\psi_{s,\mathrm{lim}}^{\mathrm{sf}} < 40$ mVs. Provided a slew-rate of $v_{d,\mathrm{lim}}^{\mathrm{sf}} = 50$ Vs/s, (12) suggests that the worst-case flux-linkage undershoot before the ASC is 25 mVs, which is considered acceptable. To remain in slew-rate until the application of the ASC, (11) stipulates $\psi_{s,\mathrm{SR}} < -13$ mVs when only considering the controller's P-term. In this case, it is expected that $(\psi_{s,0} - \psi_{s,\mathrm{lim}}^{\mathrm{sf}})/v_{d,\mathrm{lim}}^{\mathrm{sf}} = 3.2$ ms elapses before the ASC can be applied, when starting from the considered MTPA operating condition. In the drive, $\psi_{s,\mathrm{SR}}$ was set to

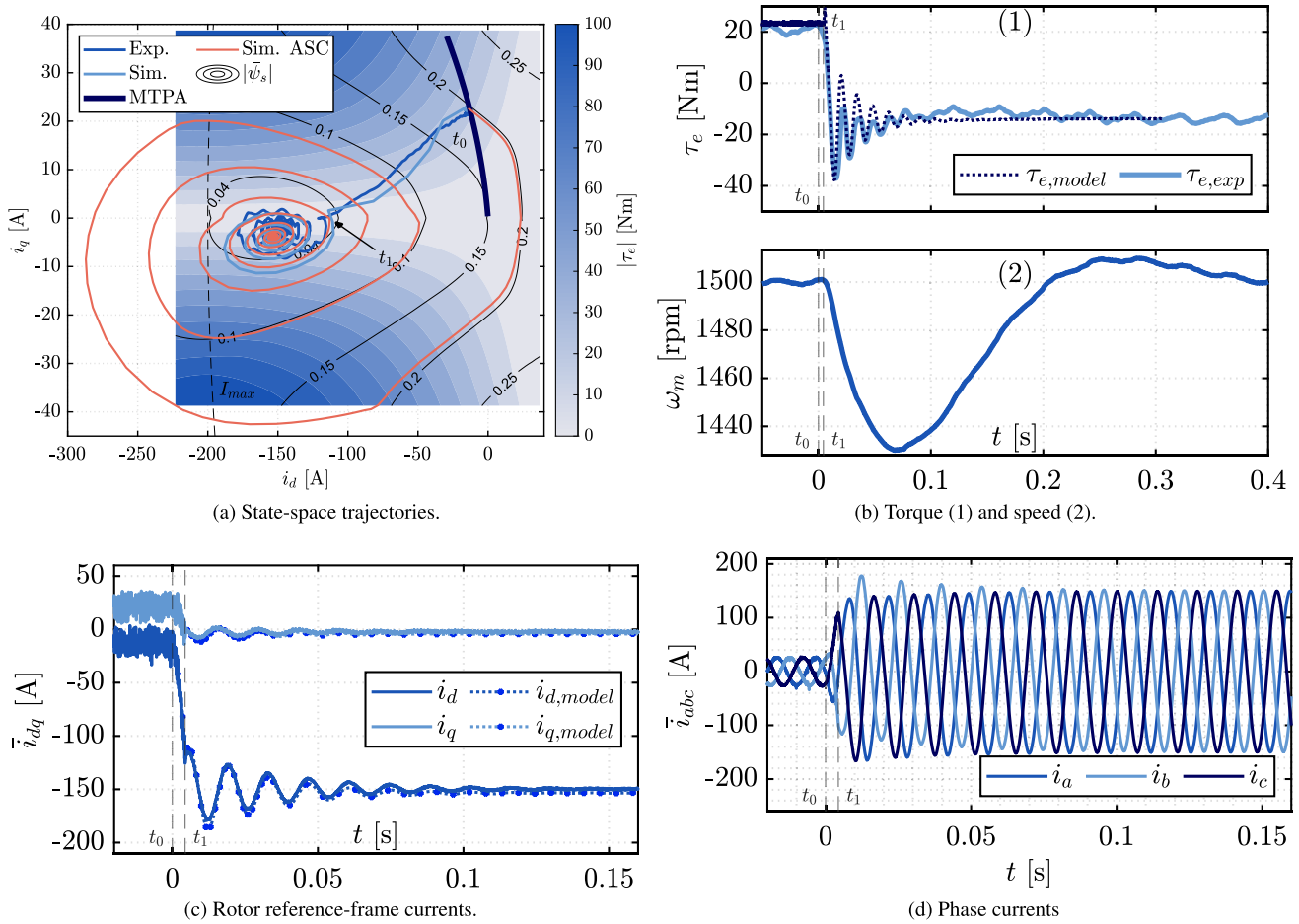

(a) State-space trajectories.

(b) Torque (1) and speed (2).

(c) Rotor reference-frame currents.

(d) Phase currents

FIGURE 14. The proposed ASC strategy implemented from a starting operating point of τ_e =21 Nm at ω_m =1500 rpm in DFVC with $\psi_{s,SOA}$ = 40 mVs. The fault triggers at $t_0 = 0$ whereas the ASC is applied at t_1 = 4.4 ms in the experiment, and at t_1 = 4.0 ms in the simulation. The flux-linkage contours indicate that the ASC is initiated at t_1 once $\psi_{s,SOA}$ is reached (Exp. and Sim.). In contrast, simulating a direct application of an ASC at t_0 violates the SOA and results in a drastic increase of peak current and torque (Sim. ASC). The magnetic model is assumed linear outside of the experimentally identified flux-maps.

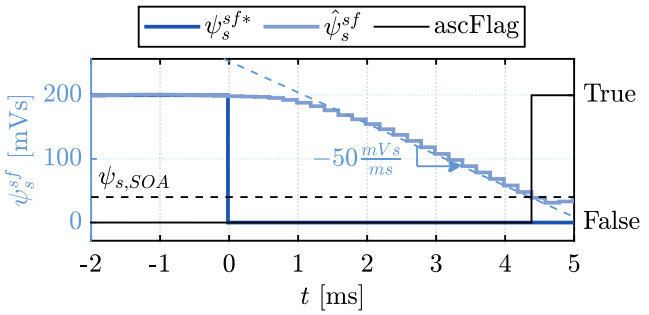

FIGURE 15. ψ_s^{sf} reduction into the SOA upon a fault, as observed by the drive using the flux observer in Fig. 9.

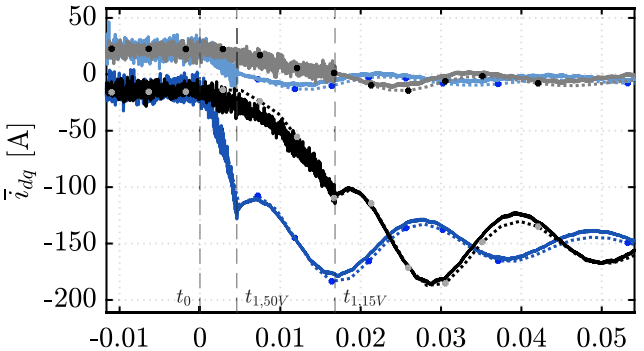

FIGURE 16. Slew-rate comparisons starting from [τ_e = 21 Nm, ω_m = 1500 rpm] at MTPA. Solid lines: measured. Dotted lines with markers: simulated. $v^{sf}_{s,lim}$ = 50 V: i_d (blue) and i_q (sky). $v^{sf}_{s,lim}$ = 15 V: i_d (black) and i_q (gray). The times to reach the SOA are $t_{1,50V}$ = 4.4 ms and $t_{1,15V}$ = 16.6 ms.

0 mVs, since an integral term also is added to the flux-linkage controller.

Fig. 14 shows the outcome of the suggested strategy from time t_0, when the fault is detected, and forward in terms of torque and current. The time domain plots in Fig. 14b and 14c indicate that the current and torque remain well within the bounds and that the ASC can be applied after t_1 = 4.4 ms. Additionally, Fig. 14d displays the phase currents for the same course. The state-space plot of Fig. 14a

makes the controlled part of the transient between t_0 and t_1 more clear. As seen, the $\bar{i}_{dq}$-trajectory crosses the iso-flux-linkage lines almost perpendicularly (i.e. in the direction of steepest descent) before commencing the familiar spiral towards the SSC once the ASC is applied. The time-domain flux linkage during the controlled flux reduction, as observed by the drive using the flux observer in Fig. 9, is displayed in greater detail in Fig. 15. It reveals that the flux-linkage reduction is in the slew-rate limit after approximately nine PWM periods. The delayed response can, in part, be attributed to the effect of the integral term and, in part, to the PWM delay.

For comparison, the simulated trajectories have been obtained by imposing the speed profile of Fig. 14b in syreDrive to account for the varying speed. Indeed, the torque reverses with approximately 60 % of the nominal torque of the DM whose speed controller also has a limited bandwidth. However, the speed dip is exacerbated by the low inertia of the test bench relative to an automobile; approximately $0.133\,\mathrm{kg\,m^2}$ from the nameplate of the DM and the MUT. Overall, the simulated response corresponds well with the measurements but exhibits a slightly lower current and torque damping. It is also perceived that the ASC initiates almost concurrently in the simulation and the experiment, with $t_1 = 4.0\,\mathrm{ms}$ in the simulation being 0.4 ms faster than in the experiment.

Finally, Fig. 16 illustrates the effect of assigning different voltage limits to the d_s-axis when starting the flux-reduction from the operating point [$\omega_m = 1500\,\mathrm{rpm}$, $\tau_e = 21\,\mathrm{Nm}$] on the MTPA curve. The figure highlights the time-domain current waveforms during the actively controlled part from the raised fault flag at t_0 to the application of the ASC at $t_{1,v^{\mathrm{sf}}_{d,\mathrm{lim}}}$ for $v^{\mathrm{sf}}_{d,\mathrm{lim}} = 50\,\mathrm{V}$ and 15 V. Since $i^{\mathrm{sf}*}_q$ is fixed and the ASC initiates at the same threshold level of the flux-linkage, the two cases are time-shifted replicas relative to time t_1. The experiment also shows that the ratio $t_{1,15V}/t_{1,50V} = 3.79$ is close to the ratio $50\,\mathrm{V}/15\,\mathrm{V} = 3.33$, indicating an almost inverse proportionality between the available voltage and the duration for reaching the SOA, as expected from (9a) for an adequately tuned controller with an appropriate value of $\psi_{s,\mathrm{SR}}$, according to (11).

VI. CONCLUSION

This paper introduces a fast and easily interpretable mathematical/graphical method for determining the SOA of initial conditions upon the application of an ASC on three-phase PMSMs. It is defined by a set of initial $\bar{i}_{dq}$ values that ensure ASC transients adhere to demagnetization current, inverter limits, and user-defined maximum torque limits. The method utilizes an inductance-based nonlinear model based on flux maps. A few offline dynamical simulations determine the entire SOA at a fixed speed, reducing computational load. The SOA boundary is shown to approximately correspond to a fixed stator flux-linkage level, and the paper discusses the impacts of speed variations.

By directing the current vector in FOC or the stator flux magnitude in DFVC within the SOA before applying an ASC, PM demagnetization can be prevented and passenger safety ensured. A DFVC-based strategy is elaborated with minimal code additions that can be seamlessly integrated into existing control code. Tuning the transition duration into the SOA is achieved by specifying the flux-decay rate. Validation on a 35 kW commercial PMSM demonstrates the model's accuracy and the pre-ASC control strategy's applicability to real-world drives. The presented method and control strategy are expected to be useful in the development, commissioning, and deployment of PMSMs in automotive applications, ensuring compliance with functional safety standards.

REFERENCES

[1] *International Organization for Standardization*, document ISO26262-1:2018, 2018. [Online]. Available: https://www.iso.org/standard/68383.html

[2] S. Chen, X. Hao, C. Gao, and Z. Jiang, "An effective nontransient active short-circuit method for PMSM in electric vehicles," *IEEE Trans. Ind. Electron.*, vol. 70, no. 4, pp. 3571–3580, Apr. 2023, doi: 10.1109/TIE.2022.3176315.

[3] G. Choi and T. M. Jahns, "Investigation of key factors influencing the response of permanent magnet synchronous machines to three-phase symmetrical short-circuit faults," *IEEE Trans. Energy Convers.*, vol. 31, no. 4, pp. 1488–1497, Dec. 2016, doi: 10.1109/TEC.2016.2594223.

[4] B. A. Welchko, T. M. Jahns, W. L. Soong, and J. M. Nagashima, "IPM synchronous machine drive response to symmetrical and asymmetrical short circuit faults," *IEEE Trans. Energy Convers.*, vol. 18, no. 2, pp. 291–298, Jun. 2003, doi: 10.1109/TEC.2003.811746.

[5] S. Ferrari, G. Dilevrano, P. Ragazzo, P. Pescetto, and G. Pellegrino, "Fast determination of transient short-circuit current of PM synchronous machines via magnetostatic flux maps," *IEEE Trans. Ind. Appl.*, vol. 59, no. 4, pp. 4000–4009, Jul. 2023, doi: 10.1109/TIA.2023.3265952.

[6] T. M. Jahns and V. Caliskan, "Uncontrolled generator operation of interior PM synchronous machines following high-speed inverter shutdown," *IEEE Trans. Ind. Appl.*, vol. 35, no. 6, pp. 1347–1357, Nov. 1999, doi: 10.1109/28.806049.

[7] Y. Du, L. Wu, H. Zhan, and Y. Fang, "Influence of dimensional parameters on three-phase short circuit and demagnetization in surface-mounted PM machines," *IEEE Trans. Energy Convers.*, vol. 36, no. 3, pp. 2514–2523, Sep. 2021, doi: 10.1109/TEC.2021.3051140.

[8] K. Lu, Y. Zhu, Z. Wu, and M. Xiao, "Suppression of current fluctuations and the brake torque for PMSM shutoff in electric vehicles," *Math. Problems Eng.*, vol. 2019, pp. 1–13, Sep. 2019, doi: 10.1155/2019/5026316.

[9] G. Falk Olson, S. Ferrari, A. Bojoi, P. Pescetto, L. Peretti, and G. Pellegrino, "Guaranteed torque and demagnetization current during active short circuit transients of PMSMs," in *Proc. 25th IEEE Int. Conf. Ind. Technol. (ICIT)*, Mar. 2024, pp. 1–8.

[10] S. Ferrari, P. Ragazzo, G. Dilevrano, and G. Pellegrino, "Flux and loss map based evaluation of the efficiency map of synchronous machines," *IEEE Trans. Ind. Appl.*, vol. 59, no. 2, pp. 1500–1509, Mar. 2023, doi: 10.1109/TIA.2022.3221381.

[11] E. Armando, R. I. Bojoi, P. Guglielmi, G. Pellegrino, and M. Pastorelli, "Experimental identification of the magnetic model of synchronous machines," *IEEE Trans. Ind. Appl.*, vol. 49, no. 5, pp. 2116–2125, Sep. 2013, doi: 10.1109/TIA.2013.2258876.

[12] *BRUSA Elektronik AG*. Accessed: Nov. 24, 2023. [Online]. Available: https://www.brusa.biz/portfolio/hsm1-6-17-12-2/

[13] P. Pescetto and G. Pellegrino, "Sensorless standstill commissioning of synchronous reluctance machines with automatic tuning," in *Proc. IEEE Int. Electr. Mach. Drives Conf. (IEMDC)*, Miami, FL, USA, May 2017, pp. 1–8, doi: 10.1109/IEMDC.2017.8002302.

[14] J. Pyrhonen, T. Jokinen, and V. Hrabovcová, *Design of Rotating Electrical Machines*. Hoboken, NJ, USA: Wiley, 2013, pp. 331–494, doi: 10.1002/9781118701591.ch7.

[15] G. Pellegrino, R. I. Bojoi, and P. Guglielmi, "Unified direct-flux vector control for AC motor drives," *IEEE Trans. Ind. Appl.*, vol. 47, no. 5, pp. 2093–2102, Sep. 2011, doi: 10.1109/TIA.2011.2161532.

[16] A. Varatharajan, G. Pellegrino, and E. Armando, "Direct flux vector control of synchronous motor drives: Accurate decoupled control with online adaptive maximum torque per ampere and maximum torque per volts evaluation," *IEEE Trans. Ind. Electron.*, vol. 69, no. 2, pp. 1235–1243, Feb. 2022, doi: 10.1109/TIE.2021.3060665.

[17] F. Cupertino and G. Pellegrino. *SyR-e: Synchronous Reluctance (Machines)-Evolution*. Accessed: Nov. 24, 2023. [Online]. Available: https://github.com/SyR-e

[18] A. Varatharajan, D. Brunelli, S. Ferrari, P. Pescetto, and G. Pellegrino, "SyreDrive: Automated sensorless control code generation for synchronous reluctance motor drives," in *Proc. IEEE Workshop Electr. Mach. Design, Control Diagnosis (WEMDCD)*, Apr. 2021, pp. 192–197, doi: 10.1109/WEMDCD51469.2021.9425649.

[19] A. Bojoi, S. Ferrari, P. Pescetto, and G. Pellegrino, "Advanced circuital model for e-drive simulation, including harmonic effects and fault scenarios," in *Proc. PCIM Eur., Int. Exhib. Conf. Power Electron., Intell. Motion, Renew. Energy Energy Manage.*, May 2023, pp. 1–10, doi: 10.30420/566091220.

GUSTAF FALK OLSON (Graduate Student Member, IEEE) was born in Kristinehamn, Sweden. He received the Diploma degree from the School of Industrial Technology and Management, and the M.Sc. degree in electrical power engineering from the KTH Royal Institute of Technology, Stockholm, Sweden, in 2016, where he is currently pursuing the Ph.D. degree in parameter estimation of multiphase electrical machines with the Division for Electrical Power and Energy Systems (EPE). After graduation, he was a Field Application Engineer with Texas Instruments. His research interests include modeling, control, and parameter estimation of electrical machines. He was the Best Student of the Year during the Diploma studies.

ANDREI BOJOI (Graduate Student Member, IEEE) received the B.Sc. and M.Sc. degrees in electrical engineering from the Politecnico di Torino, Italy, in 2019 and 2022, respectively, where he is currently pursuing the Ph.D. degree with the Dipartimento Energia "G. Ferraris." He is a member of the Power Electronics Innovation Center (PEIC), Politecnico di Torino. His main research interests include advanced modeling solutions and control of synchronous electrical machines, in particular on synchronous reluctance and permanent magnet machines.

PAOLO PESCETTO (Member, IEEE) received the M.Sc. and Ph.D. degrees (Hons.) from the Politecnico di Torino, Turin, Italy, in 2015 and 2019, respectively. He is an Assistant Professor with the Politecnico di Torino. Since Fall 2019, he has been a Researcher and a tenure-track Lecturer with the Energy Department, Politecnico di Torino, where he is also a member of the Power Electronics Innovation Center (PEIC). In 2014, he was an Erasmus Student with the Norwegian University of Science and Technology, Trondheim, Norway. He has authored or co-authored more than 40 scientific works, with 14 IEEE journal articles and two patents. His research interests include synchronous motor drives, sensorless control, self-commissioning techniques, thermal models, and integrated battery chargers for EVs. He received five IEEE paper awards and two IEEE Ph.D. thesis awards. Since Fall 2022, he has been the Vice Chair of the IEEE IA/IE/PEL North Italy Joint Chapter.

SIMONE FERRARI (Member, IEEE) receive the Ph.D. degree (cum laude) from the Politecnico di Torino, in 2020. He is currently an Assistant Professor with the Politecnico di Torino. From July to December 2018, he was a Visiting Scholar with North Carolina State University, Raleigh, NC, USA. He is one of the authors of SyR-e, an open-source environment for synchronous reluctance and permanent magnet machines design and analysis. His research interests include electrical machine design and testing, with a focus on synchronous reluctance and permanent magnet machines.

LUCA PERETTI (Senior Member, IEEE) received the M.Sc. degree in electronic engineering from the University of Udine, Italy, in 2005, and the Ph.D. degree from the University of Padova, Italy, in 2009. From November 2007 to March 2008, he was a Visiting Ph.D. Student with ABB Corporate Research, Sweden, where he was a Principal Scientist, a Project Leader, and a Strategy Coordinator, from August 2010 to August 2018. He has also been an Affiliated Faculty Member with the Division of Electric Power and Energy Systems, KTH, since July 2016, where he has been an Associate Professor of electric machines and drives, since September 2018. His main scientific interests include the automatic parameter estimation in electric machines, sensorless control, loss segregation in drive systems, multiphase drives, condition monitoring of machines and drives, in the context of industrial, wind energy, and traction applications.

GIANMARIO PELLEGRINO (Fellow, IEEE) is currently a Professor of power converters, electrical machines, and drives with the Politecnico di Torino, Turin, Italy. He was a Visiting Fellow with Aalborg University, Aalborg, Denmark; the University of Nottingham, Nottingham, U.K.; and the University of Wisconsin–Madison, Madison, WI, USA. He has authored the open-source platform SyR-e for the design of electrical motors and drives, constantly developed and validated in the context of collaborations with the industry and widely adopted worldwide. He has co-authored more than 60 IEEE journal articles and nine patents. He was a recipient of the Eighth Grand Nagamori Award. He received nine best paper awards. He is a Founding Member of the Power Electronics Interdepartmental Center (PEIC), Politecnico di Torino; a member of the Advisory Board of PCIM Europe; and the Adjunct Vice Rector of technology transfer with the Politecnico di Torino. He is an Associate Editor of IEEE TRANSACTIONS ON INDUSTRY APPLICATIONS.